Charge-spin conversion in layered semimetal $TaTe_2$ and spin injection in van der Waals heterostructures

Anamul Md. Hoque, Dmitrii Khokhriakov, Bogdan Karpiak, and Saroj P. Dash*
Department of Microtechnology and Nanoscience, Chalmers University of Technology, SE-41296, Göteborg, Sweden

(Received 5 December 2019; accepted 17 June 2020; published 6 August 2020)

A spin-polarized current source using nonmagnetic layered materials is promising for next-generation all-electrical spintronic science and technology. Here we electrically created spin polarization in a layered semimetal $TaTe_2$ via the charge-spin conversion process. Using a hybrid device of $TaTe_2$ in a van der Waals heterostructure with graphene, the spin polarization in $TaTe_2$ is efficiently injected and detected by nonlocal spin-switch, Hanle spin precession, and inverse spin Hall effect measurements. Systematic experiments at different bias currents and gate voltages in a vertical geometry prove the $TaTe_2$ as a nonmagnetic spin source at room temperature. These findings demonstrate the possibility of making an all-electrical spintronic device in a two-dimensional van der Waals heterostructure, which can be essential building blocks in energy-efficient spin-orbit technology.

DOI: 10.1103/PhysRevResearch.2.033204

I. INTRODUCTION

Spintronic technology was mainly governed by the generation of spin-polarized currents by using the exchange interaction of conduction electrons in magnetic materials, which require a magnetic field to control their spin orientation [1–4]. However, the demand for faster and smaller spintronic technologies for memory, logic, and artificial intelligence requires efficient and spontaneous spin-polarized current sources using nonmagnetic materials, where all the device operations can be controlled by electrical means [5,6]. Recently, the electronic generation of spin-polarized currents was realized in nonmagnetic materials via the spin Hall effect (SHE), Rashba-Edelstein effect (REE), and spin momentum locking (SML) phenomenon [7–9].

Due to their potential for spintronic applications, the SHE and REE were extensively studied in heavy metals [10,11], semiconductors, oxide heterostructures [7], and more recently, on transition metal dichalcogenides (TMDs) [12], Weyl semimetals [12,13], Rashba spin-orbit materials [14], and their heterostructures with graphene [12,13,15–18]. Topological insulators (TIs) were shown to possess SML characteristics in the Dirac surface states, which could be detected using potentiometric measurements [19–21] and the charge-spin conversion process [22–24]. However, the spin injection from TIs into graphene is so far restricted to very low temperatures due to contributions from trivial bulk states [25,26]. Utilizing the SHE in Pt metal thin films, spin injection and detection has been realized in a graphene channel [10,11]. However, the direct deposition of metallic layers on graphene can modify its electronic properties [27,28]. Recently discovered two-dimensional (2D) magnets can be potential candidates for spin injection into graphene; however, the low Curie temperature of the 2D magnets at this stage limits their room-temperature applications [29]. Therefore, finding a nonmagnetic layered material as a spin source in a van der Waals (vdW) heterostructure with graphene is necessary for newly emerging 2D spintronics science and technology [30].

Using our recently developed vertical measurement geometry [13], we demonstrate the electronic creation and injection of in-plane spin polarization using a layered semimetal tantalum ditelluride ($TaTe_2$) due to efficient charge-spin conversion processes. In a hybrid spintronic device, the spin polarization generated in $TaTe_2$ is efficiently injected into the graphene channel and subsequently detected by a ferromagnet using a sensitive nonlocal spin-valve and Hanle spin precession measurements. Detailed measurements using different bias currents and gate voltages provide insight into the current-induced spin polarization in $TaTe_2$ at room temperature.

II. RESULTS AND DISCUSSION

The choice of the layered monoclinic (1T') semimetal $TaTe_2$ is motivated by its high spin-orbit interaction (SOI) originating from 5*d* electrons along with the potential for use in charge-to-spin conversion technologies [7,31], and it can be exfoliated into thin 2D layers. Mainly, $TaTe_2$ is an excellent candidate for the generation of pure spin current due to SHE [7,32] and REE [9,33,34], as shown schematically in Fig. 1(a). Figure 1(b) shows the fabricated device picture, where a vdW heterostructure of $TaTe_2$ is prepared with a graphene channel to use its excellent spin transport properties [35,36] together with ferromagnetic Co/TiO_2 (FM) injector/detector tunnel contacts (see Appendix A for detailed fabrication processes). The characteristic Raman spectrum of a $TaTe_2$

*Corresponding author: saroj.dash@chalmers.se

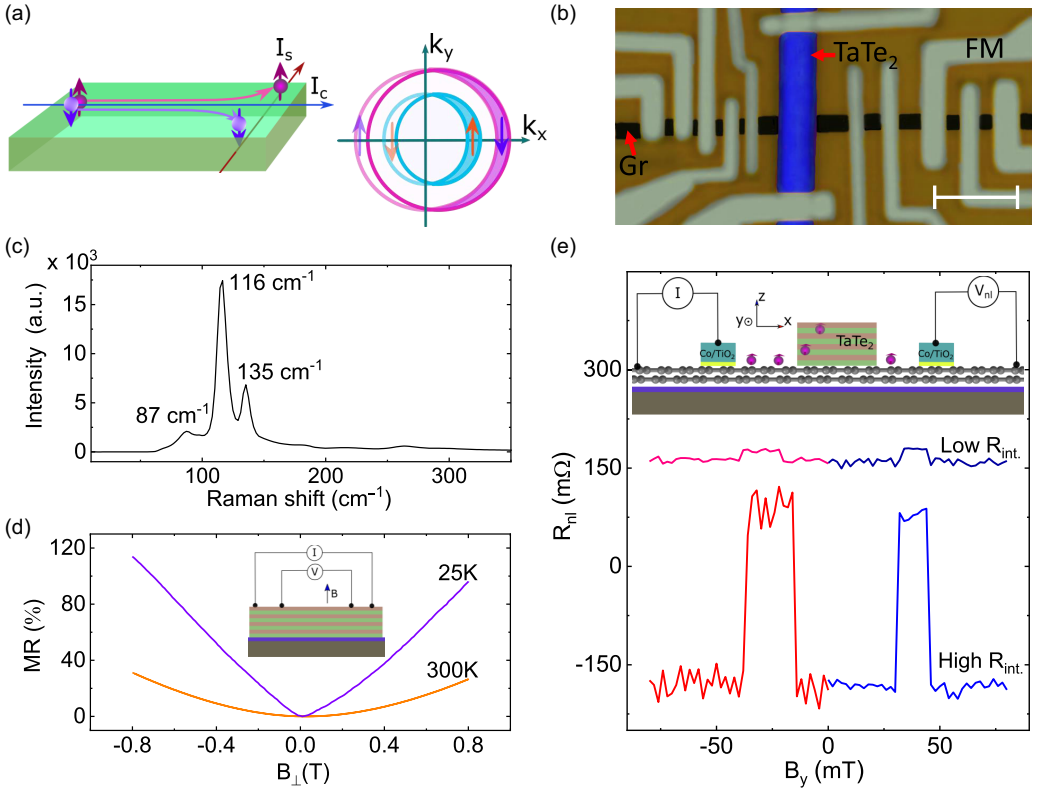

FIG. 1. Characterization of $TaTe_2$ and spin transport in the graphene-$TaTe_2$ heterostructure. (a) Schematic representation of the spin Hall effect in a symmetric system, where a spin current (I_s) is created due to transverse charge current (I_c). The adjacent diagram shows the current-induced spin polarization in Rashba spin-split bands near the Fermi level. (b) Optical micrograph with false colors of a device consisting of graphene (black), $TaTe_2$ (blue), and FM contacts (gray). The scale bar is 4 μm. (c) Raman spectrum of $TaTe_2$ at room temperature. (d) Magnetoresistance (MR%) of $TaTe_2$ at room temperature and 25 K. (e) Nonlocal spin-valve (NLSV) signal without and with spin absorption in the high-R_{int} and low-R_{int} conditions, respectively. The inset shows the NLSV measurement geometry.

flake is shown in Fig. 1(c) using a 638-nm laser, where three prominent peaks at 87, 116, and 135 cm^{-1} are visible [31]. In the transport measurements, $TaTe_2$ shows semimetallic properties (see Appendix B) and a large magnetoresistance ($MR\ \% = \frac{R_B - R_0}{R_0} \times 100$) [Fig. 1(d)], showing MR ∼30% at room temperature and ∼120% at 25 K at a magnetic field of −0.8 T [37].

Standard nonlocal (NL) spin-valve measurements were performed across the graphene-$TaTe_2$ heterostructure channel in different graphene-$TaTe_2$ interface resistance (R_{int}) conditions [Fig. 1(e)]. The spin-polarized electrons were injected and detected by FM contacts in the NL geometry while measuring a $\Delta R_{nl} = (\frac{\Delta V_{nl}}{I})$ as a function of magnetic field sweep (B_y) to achieve the parallel and antiparallel magnetization of FM electrodes. As shown in Fig. 1(e), while a large spin transport signal ΔR_{nl} of 272 mΩ was measured for high R_{int} of 16 kΩ, for very low R_{int}, tentatively < 100 Ω (see Appendix C), the ΔR_{nl} drastically reduced to 16 mΩ due to strong spin absorption in the low-R_{int} regime.

First, the spin-to-charge conversion experiments [measurement geometry in Fig. 2(a)] were performed in $TaTe_2$ via the inverse spin Hall effect (ISHE), when the R_{int} is <100 Ω (see Appendix C). In this condition, the spin current injected from a FM into the graphene channel is strongly absorbed by $TaTe_2$, as shown in Fig. 1(e). The spin current in $TaTe_2$ subsequently gives rise to a transverse charge current due to the efficient spin-charge conversion in $TaTe_2$, which is detected as a voltage signal (V_{nl}) across the $TaTe_2$ [Fig. 2(b)]. By sweeping an in-plane magnetic field along the x axis, B_x, the V_{nl} varies antisymmetrically at low field and saturates at ±0.4 T as the magnetization of the injector FM rotates completely toward the x axis. The saturation field range of the FM contacts for the B_x field sweep has been verified from the spin precession x-Hanle measurements in the graphene channel (see Appendix D). Considering the symmetry of the system with the spin current being absorbed from graphene into $TaTe_2$ along the z direction, spin polarization (⩾0.4 T) in the x direction and manifested orthogonal charge current (I_s) in the y direction can be due to the ISHE or the Edelstein effect (EE) in $TaTe_2$ [12]. The V_{nl} signal has been measured at different spin injection bias currents, which scales linearly [Fig. 2(c)] at room temperature.

We observed a large spin-charge conversion (SCC) signal at room temperature in $TaTe_2$ with signal amplitude $\Delta R_{SCC} = \Delta V_{nl}/I_{bias} = -1.69\mu V/-20\,\mu A \sim 84\,m\Omega$, which is about few times larger than in WTe_2 [12], MoS_2, and Pt in heterostructure with graphene [10,11,17], one order of magnitude larger than in graphene-$MoTe_2$ heterostructure [38], and a few orders of magnitude higher than in Pt/Cu heterojunction [39] but comparable to the graphene-TaS_2 heterostructure system [15]. Recently, spin-orbit torque experiments using a $TaTe_2$-ferromagnet heterostructure reported a dominating

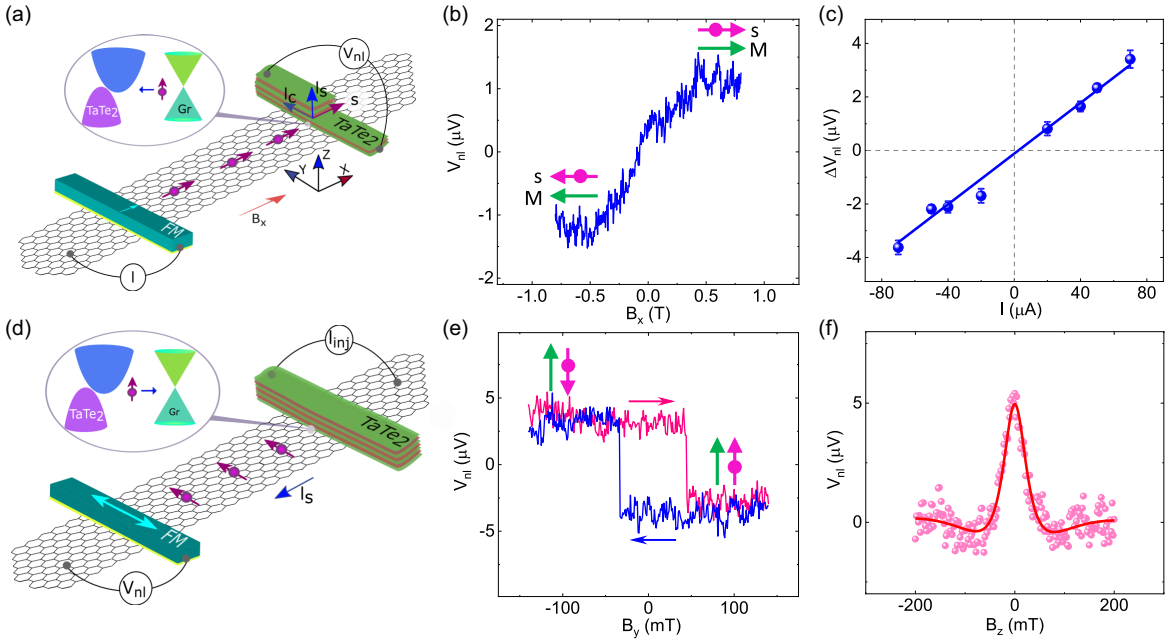

FIG. 2. Charge-spin conversion effects in $TaTe_2$ at room temperature. (a) Measurement geometry to detect the inverse spin Hall effect (ISHE) in $TaTe_2$ by injecting a spin current from the ferromagnet-graphene channel into $TaTe_2$ by spin absorption and detecting a voltage signal across the $TaTe_2$ in a NL geometry. (b) ISHE signal V_{nl} measured with an in-plane magnetic field (B_x) sweep for $I = 50\,\mu$A at $V_g = 40$ V at room temperature in device 1. (c) Bias current dependence of the ISHE signal amplitude ΔV_{nl} with a linear fit (solid line). (d) Measurement geometry where $TaTe_2$ is used as a spin-polarized current source for vertical injection of spins into the graphene channel, which is finally detected by a FM contact in a NL geometry. (e, f) The spin-switch and Hanle spin precession measurements for spin injection from $TaTe_2$ with a B_y and B_z sweep, respectively, with an application of an $I = -30\,\mu$A with $V_g = 40$ V at room temperature in device 2. The up and down magnetic field sweep directions are indicated by arrows in (e) for spin-switch experiments. The Hanle data is fitted using Eq. (2). A linear background is subtracted from the data.

Oersted field contribution by local measurements [40], which is avoided in our NL measurements. Form our data, it is not possible to calculate the exact spin Hall angle (θ_{SH}) in $TaTe_2$, as the spin diffusion length λ_{TaTe_2}, is unknown. Furthermore, the larger width of a $TaTe_2$ flake (2.6 μm) compared to the spin diffusion length in graphene (∼2.5 μm) restrains the use of the available model [10–12]. An estimation of θ_{SH} was found to be in the range of 0.2–0.6 using a simple model and considering $\lambda_{TaTe_2} = 10$–110 nm and R_{int} of 10–100 Ω (see Appendix E). Moreover, we have also approximately calculated the inverse Edelstein effect (IEE) of $TaTe_2$ through IEE length $\lambda_{IEE} = \theta_{SH} * \lambda_{TaTe_2}$, and we found $\lambda_{IEE} \approx 6$–60 nm (see Appendix E for more discussion) as a function of λ_{TaTe_2} (10–110 nm).

Next, we focus on the observation of vertical spin injection (VSI) of in-plane spin polarization from $TaTe_2$ into a graphene channel at room temperature [see Fig. 2(d) for measurement geometry]. In the spin-switch experiment, we measured the spin signal V_{nl} as a function of an in-plane magnetic field B_y sweep, which switches the magnetization of the FM detector contact from parallel to antiparallel orientation with respect to the in-plane injected spin polarization from $TaTe_2$ [Fig. 2(e)]. The amplitude ($\Delta R_{nl} = \Delta V_{nl}/I_{bias}$) of the spin-to-charge conversion signal for vertical spin injection is about 240 mΩ. A confirmatory test of the in-plane spin polarization using a Hanle spin precession measurement was performed in the same NL geometry [Fig. 2(d)], where a perpendicular magnetic field (B_z) was swept while keeping the magnetization of the detector FM contact in the in-plane orientation. The B_z field induces spin precession in addition to diffusion and dephasing, which results in a reduction of the spin signal as the detector probes only the projection of the spin orientation onto the FM contact. Figure 2(f) shows the Hanle data measured at room temperature while injecting spin from $TaTe_2$ into the graphene channel, and fitting with Eq. (F1), we estimate the spin lifetime $\tau_s = 195 \pm 26$ ps and spin diffusion length $\lambda_s = \sqrt{\tau_s D_s} = 1.98 \pm 0.3\mu$m, considering the channel length between the $TaTe_2$ and detector FM electrode $L = 3.75\,\mu$m (distance between the center of the $TaTe_2$ flake to the center of the FM electrode). We found the spin polarization of the FM detector contact is about $P_{FM} \sim 6.13\%$ (Fig. 10). Subsequently, knowing the P_{FM}, the lower limit for the current-induced spin polarization of $TaTe_2$ is calculated to be about $P_{TaTe_2} = 1.34\% \pm 0.26\%$ (see Appendix F).

We further investigated the back-gate (V_g) dependence of the VSI spin-switch signal using $TaTe_2$ as the spin injector. Figure 3(a) shows a sketch of the graphene-$TaTe_2$ heterostructure and the change in the Fermi-level position in graphene with an application of V_g from electron- to hole-doped regimes, whereas no change is expected in $TaTe_2$ due to its metallic state. The measured spin-switch signals (V_{nl}) at various V_g in the range from −40 to 40 V are depicted in Fig. 3(b). The gate dependence of the magnitude of the spin signal ΔV_{nl}($\Delta R_{nl} \approx 250$–$400$ mΩ) is presented in Fig. 3(c) (top panel), which shows that the spin-switch signal direction remains unchanged in the hole and electron transport regime.

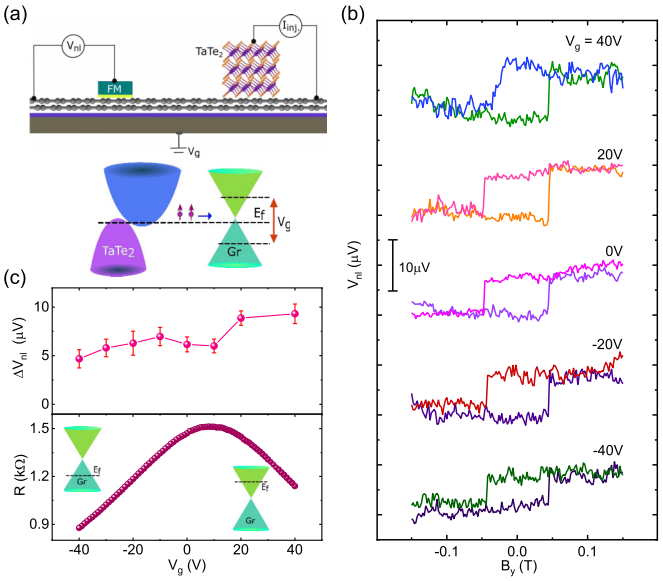

FIG. 3. Gate dependence of spin injection signal from $TaTe_2$. (a) Measurement setup and the band diagram of $TaTe_2$ and graphene with an application of a back-gate voltage (V_g) across the Si/SiO_2 substrate. (b) The measured NL spin-switch signals at various $V_g = -40$–40 V for both n- and p-doped graphene regime in device 3 with a bias current $I = -20\,\mu$A at room temperature. (c) The magnitude of the signal ΔV_{nl} as a function of V_g (top panel). The V_g dependence of the graphene-$TaTe_2$ heterostructure channel resistance (bottom panel) along with the Fermi-level position in the graphene band structure.

To compare ΔV_{nl} with the heterostructure channel properties, the gate dependence of the graphene-$TaTe_2$ heterostructure channel resistance is presented in the bottom panel of Fig. 3(c), where the charge neutrality point (V_{CNP}) is $\sim$10 V with field-effect mobility of about 1074 $cm^2\ V^{-1}\ s^{-1}$. Similar gate dependence of the spin-switch signal is observed for device 1 (see Appendix G). These results rule out any contribution of the local Hall effect produced by the local fringe field from the FM detector contact edges on the graphene, since this effect should change its sign with carrier types in graphene [41].

Next, the electrical-bias-controlled switching of the spin injection from $TaTe_2$ was measured. Figure 4(a) shows the spin-switch signal (V_{nl}) with injection bias currents of $I = +/-2\,\mu$A at $V_g = 20$ V. Reversing the current direction creates opposite spin polarization in $TaTe_2$ and hence accumulation of opposite spins in the graphene channel, which results in the opposite direction of the hysteretic behavior of the measured spin-switch signal. A full bias-dependent measurement was carried out at larger biases to understand the detailed energy dependence of the spin injection mechanism at the graphene-$TaTe_2$ junction [see Figs. 4(b) and 4(c)]. In the $-I$ range, we observed an increase of ΔV_{nl} with bias currents, where the amplitude of the spin-to-charge conversion signal is about $\Delta R_{nl} = 300\text{m}\Omega$. However, for the $+I$, the ΔV_{nl} increases linearly for low biases up to $I = 8\,\mu$A and disappears at larger bias within the measurement noise. One of the reasons for such bias dependence can be ascribed to the energy dependence of spin polarization in $TaTe_2$ or the availability of spin-polarized density of states near the Fermi level in $TaTe_2$. In contrast to local detection of the spin signal [42,43], as the measurements were performed in the NL geometry without any bias across the detector FM contact, any effects originating from the detector can be ruled out. This asymmetric feature of the bias-dependent spin injection effect in graphene-$TaTe_2$ heterostructure can be correlated to an electronic diode, where instead of controlling the charge current with bias in the conventional diode we control the spin injection in the heterostructure. To further examine the asymmetry of the bias dependence, we also checked the bias dependence of the graphene-$TaTe_2$ injector interface resistance (R_{int} [see Fig. 4(d)]. Interestingly, R_{int} is observed to be asymmetric with bias, which can be the origin of the asymmetry in the spin injection signal due to a conductivity mismatch issue between the $TaTe_2$ spin source and the graphene channel [35,44].

We discuss the possible mechanisms that engender the generation of current-induced in-plane spin polarization in the $TaTe_2$ in VSI geometry. First, like the ISHE measurements, we can also explain the VSI signal in $TaTe_2$ using the symmetry principle [see Appendix H, Figs. 12(a)–12(d)], that the generated field or spin (s) is perpendicular to the applied charge current (I_c) and spin current (I_s). As the $TaTe_2$ crystals have a relatively smaller thickness (70 nm) compared to their lateral width (2.6–6 μm), as well as a low resistance compared to the graphene and interface (R_{int}), this makes the electric field within $TaTe_2$ predominantly in plane. Moreover, considering the in-plane spin injection in graphene, the origin of spin polarization can be attributed to the bulk SHE of $TaTe_2$ due to an in-plane electric field in $TaTe_2$. Similarly, the surface or bulk states of $TaTe_2$, if present and spin polarized, can also inject in-plane spin into graphene due to the EE [13] (see Fig. 12). If we consider the lower symmetry of the $TaTe_2$ crystals [40], both SHE and EE can also give rise to in-plane spin polarization in the $TaTe_2$, as it does not have to follow the orthogonal rule between s, I_c, and I_s [45]. On the other hand, proximity-induced SHE in graphene can be excluded as an origin of the signals, as it is expected to align spin in the out-of-plane direction [16–18,46]. Moreover, with the lack of gate-dependent sign change behavior of the spin-switching signal for electron and hole transport regimes, the contribution of proximity-induced REE in graphene can be ruled out [15,16,47–49]. Any contribution of spin polarization from the Te layer can also be ruled out because equal and opposite contributions from both Te surfaces within a single $TaTe_2$ layer will be canceled out [50].

III. CONCLUSION

In summary, we demonstrated efficient charge-spin conversion in semimetal $TaTe_2$ as an efficient spin injector in graphene-based spintronic devices at room temperature by using a vertical spin injection geometry. The advantage of using such a spin source is that the spin polarization direction can be controlled by an electrical bias instead of the magnetic field as conventionally achieved with ferromagnetic materials. Systematic bias and gate-dependent measurements of the spin injection signal indicate that the origin of spin polarization can be mainly because of the SHE or EE in $TaTe_2$ considering symmetric or low-symmetric spin-charge

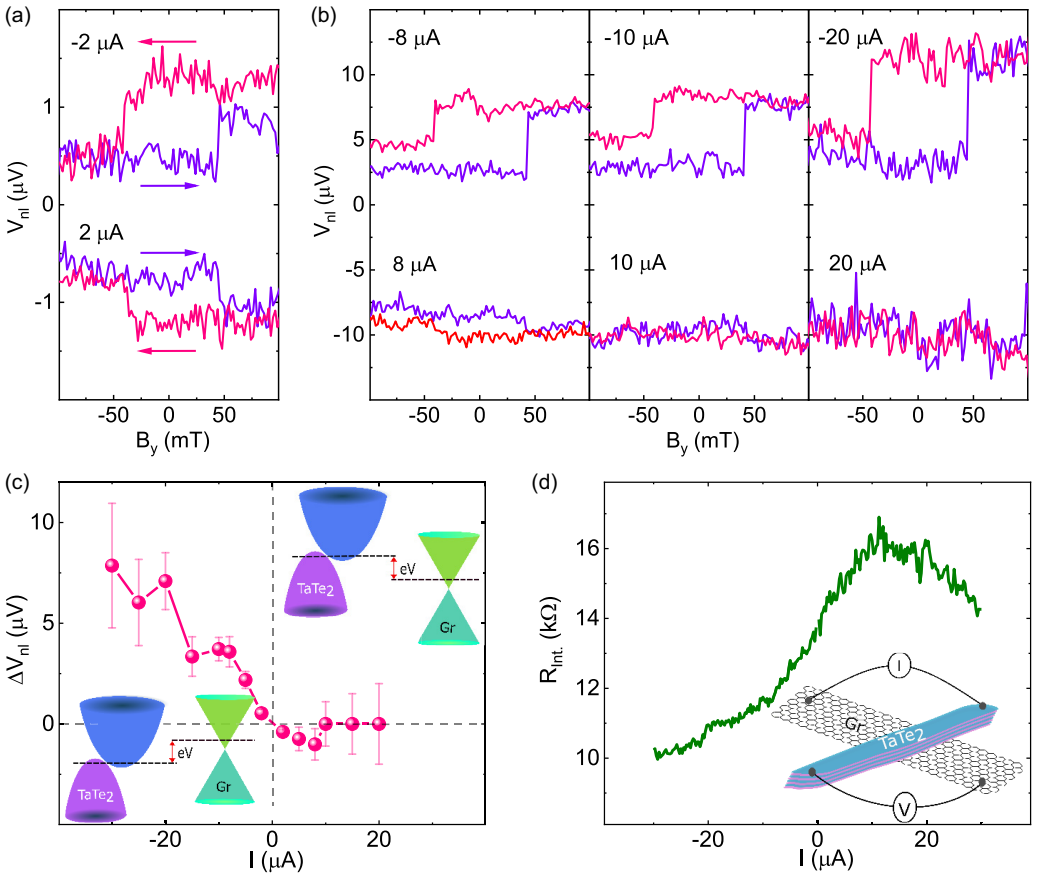

FIG. 4. Electrical control and bias dependence of spin injection signal from $TaTe_2$. (a) NL spin-switch signals (V_{nl}) with bias currents of $I = +/-2\mu$A at $V_g = 20$ V at room temperature in device 3. (b) The V_{nl} at different bias currents, measured at room temperature at $V_g = 20$ V. The data are vertically shifted for clarity. (c) Bias dependence of the magnitude of the signal ΔV_{nl}. Insets: Schematic of the nonequilibrium Fermi-level positions for positive and negative applied bias conditions. (d) Graphene-$TaTe_2$ interface resistance (R_{int}) characteristics with bias current (I) measured in four-terminal geometry (inset).

conversion processes. Such a nonmagnetic spin source based on the charge-spin conversion effect shows great potential to replace the ferromagnetic injector in all-electrical 2D spintronic circuits and is suitable for spin-orbit technologies.

ACKNOWLEDGMENTS

The authors acknowledge financial support from the European Union's Horizon 2020 Graphene Flagship Core 2 no. 785219 and Core3 no. 881603, 2DTech Vinnova Competence center at Chalmers, the EU FlagEra project (VR No. 2015-06813), and the Swedish Research Council VR project (Grant No. 2016-03658). We acknowledge the discussions and help of Bing Zhao in our research group.

APPENDIX A: FABRICATION AND CHARACTERIZATION OF GRAPHENE-$TaTe_2$ HETEROSTRUCTURE

To fabricate graphene-$TaTe_2$ heterostructure spintronic devices, first a few layer graphene were mechanically exfoliated from highly ordered pyrolytic graphite (HOPG) onto SiO_2 (300 nm)/n-doped Si substrate using the Scotch tape method. Later, $TaTe_2$ flakes were exfoliated from bulk crystal (from Hq Graphene) on polydimethylsiloxane (PDMS) film and dry transferred onto the few-layer graphene flake under a microscope using a home-built micromanipulator-controlled transfer stage. Contacts to graphene and $TaTe_2$ were defined by electron-beam lithography, electron-beam evaporation, and a lift-off process. For the preparation of ferromagnetic tunnel contacts to graphene, a two-step deposition of 0.5 nm of Ti at less than 3×10^{-7} Torr and 30 min *in situ* oxidation at above 30 Torr was carried out, followed by 90 nm of Co deposition. The resistances of ferromagnetic tunnel contacts (TiO_2/Co) on the graphene channel were in the range of 5–20 kΩs at room temperature. The spin injection measurements were performed in a vacuum cryostat with a magnetic field up to 0.8 T. All the measurements were performed at room temperature using a Keithley 6221 current source, a Keithley 2182A nanovoltmeter, and Keithley 2612B source meter for application of gate voltages.

Figures 5(a) and 5(b) show the optical microscopic picture and atomic force microscopic image of device 1 consisting of exfoliated $TaTe_2$, graphene with Co/TiO_2 tunnel contacts. The widths of the $TaTe_2$ flake and graphene stripe are 2.6 μm and 1.8 μm, respectively. After bias-dependent measurements of the inverse spin Hall effect, the flake was damaged, presumably due to gate leakage. The thickness of the exfoliated $TaTe_2$ flake is about 70 nm, scanned along the dotted orange line in the atomic force microscopy image. Figures 5(c) and 5(d) present the optical micrographs of

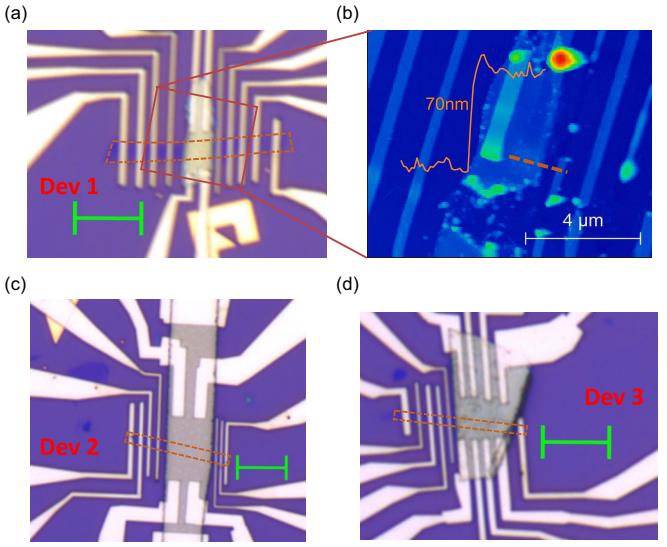

FIG. 5. (a, b) Optical microscopic picture and atomic force microscopic image of device 1 consisting of exfoliated 70 nm $TaTe_2$, graphene with Co/TiO_2 tunnel contacts. (c, d) Optical microscopic images of devices 2 and 3. The green color scale bar in the microscopic images is 6 μm.

devices 2 and 3, respectively, prepared by similar fabrication procedures. Dotted lines in the optical micrographs are to highlight the exfoliated multilayer graphene region below the $TaTe_2$ flake.

APPENDIX B: ELECTRIC AND MAGNETOTRANSPORT PROPERTIES OF $TaTe_2$

Figure 6(a) shows conventional four-terminal (4T) *I-V* characteristics of the $TaTe_2$ flake with channel resistance 120 Ω at room temperature (pink line) and 70 Ω at 25 K (green line). The resistivity ($\rho = R\frac{A}{L}$) of $TaTe_2$ is approximated to be $\sim 300 \times 10^{-8}$ Ωm at room temperature and is $\sim 60 \times 10^{-8}$ Ωm at 25 K. The $TaTe_2$ channel length (L) is 13 μm and the width (w) is 11 μm; the thickness of $TaTe_2$ is about 30 nm.

We examined the magnetoresistance (MR%) of $TaTe_2$ with angle dependence measurements up to ±0.8 T from the perpendicular (⊥) to in-plane field (ll) with respect to the device plane at 300 K with $I = -150\,\mu$A, as shown in Fig. 6(b). Figure 6(c) presents a maximum MR% at different angles at 0.8 T with a cosine fit. It can be seen [from Figs. 6(b) and 6(c)] that MR% is maximum with the out-of-plane field (Angle = 0) but turns to a minimum with an in-plane field.

APPENDIX C: INTERFACIAL RESISTANCE OF GRAPHENE-$TaTe_2$ HETEROSTRUCTURE

The graphene-$TaTe_2$ interfacial resistance (R_{int}) is estimated by two-terminal (2T) measurement geometry in device 1 [Fig. 7(a)]. At the start of the measurements, the 2T resistance was 35 kΩ [Fig. 7(b)], and the 4T R_{int} was about 16 kΩ [Fig. 4(d)]. In such a high-R_{int} condition, the spin transport in graphene is not much affected (without spin absorption). Such high resistance, in the beginning, can be due to the larger van der Waals gap between graphene and $TaTe_2$. After a few hours of measurement, we observed the 2T resistance to decrease and stabilize at ∼5 kΩ [Fig. 7(b)]. The 4T measurements could not be performed in the low-interface condition due to a lack of working contacts on both sides of the $TaTe_2$ flake. By considering the graphene channel and contact resistances, the low R_{int} is estimated to be less than 100 Ω. In this low-R_{int} condition, we observed a drastic reduction of the spin transport signal in graphene due to spin absorption by $TaTe_2$ [presented in Fig. 1(e)]. The inverse spin Hall effect measurements were performed in low-R_{int} and vertical spin injection measurements that were performed in high-R_{int} conditions.

APPENDIX D: *x*-FIELD HANLE IN GRAPHENE-$TaTe_2$ HETEROSTRUCTURE

Figure 8(a) shows a schematic of the measurement setup for nonlocal xHanle, where the magnetic field is applied in the planner perpendicular direction (x axis) to the magnetic easy axis (y axis) of the FM contacts [51]. Figure 8(b) shows the measured xHanle spin signal in a condition where $TaTe_2$ does not absorb the spin significantly. It can be seen that the magnetization of the FM becomes saturated at ±0.4 T along the x axis.

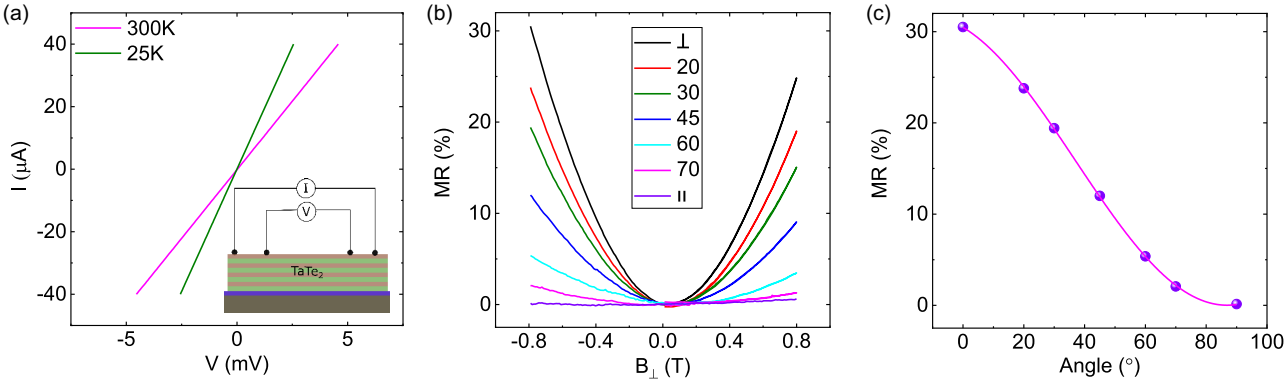

FIG. 6. Transport properties of $TaTe_2$. (a) Four-terminal (4T) *I-V* characteristics of $TaTe_2$ along with the measurement geometry. (b) Angle-dependent measurements of MR% in $TaTe_2$ from perpendicular (⊥) to the in-plane field (ll) at room temperature. (c) Maximum MR% at different angles at 0.8 T with cosine fit.

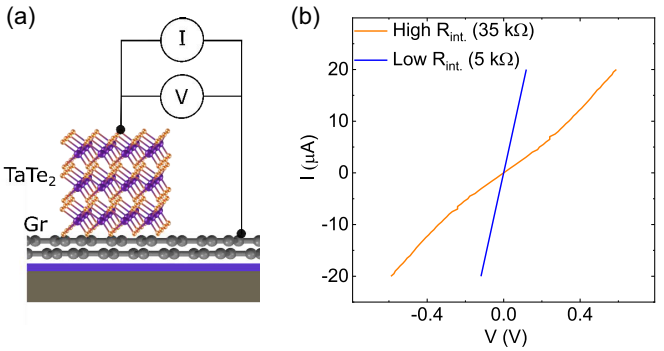

FIG. 7. Interfacial resistance in the graphene-$TaTe_2$ heterostructure. (a) Schematic of the 2T measurement geometry to measure I-V characteristics of the graphene-$TaTe_2$ heterostructure. (b) 2T I-V properties of the graphene-$TaTe_2$ heterostructure, where high resistance, 35 kΩ (orange line), and low resistance, 5 kΩ (blue line), stages are shown.

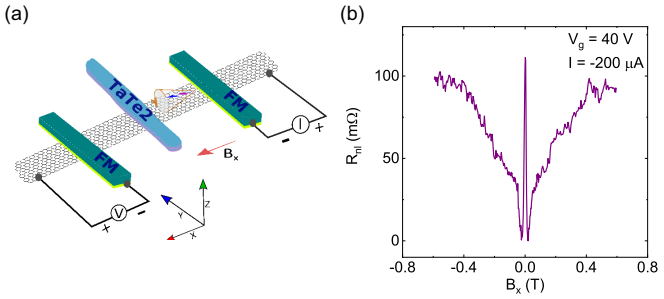

FIG. 8. x-field Hanle in graphene-$TaTe_2$ channel. (a) Schematic representation of the measurement setup to measure nonlocal xHanle, where the magnetic field is applied in the planner perpendicular direction (x axis) to the magnetic easy axis (y axis) of the FM electrodes. (b) Measured xHanle spin signal at $I = -200\,\mu$A and $V_g = 40$ V at room temperature.

APPENDIX E: ESTIMATION OF SPIN HALL ANGLE

We have estimated the spin Hall angle (θ_{SH}) in $TaTe_2$ by using the spin diffusion model [10–12]. The manifested inverse spin Hall effect (ISHE) signal can be represented using the following equation:

$$\Delta R_{\rm ISHE} = \frac{2\theta_{\rm SH}\rho_{\rm TaTe_2}X}{w_{\rm TaTe_2}}\left(\frac{\hat{I}_s}{I_c}\right). \tag{E1}$$

Here, $\Delta R_{\rm ISHE}$, $\theta_{\rm SH}$, $\rho_{\rm TaTe_2}$, X, and $w_{\rm TaTe_2}$ are the ISHE signal amplitude ($\Delta R_{\rm ISHE} = \Delta V_{\rm ISHE}/I_{50\mu A} = 43\,$mΩ), spin Hall angle, resistivity of $TaTe_2$ (300 μΩ cm), shunting factor (0.94), and width of $TaTe_2$ (2.6 μm). $\hat{I}_s$ and I_c are the effective spin current absorbed by $TaTe_2$ from the graphene channel due to the shunting effect and converted charge current due to ISHE in $TaTe_2$. The shunt factor (X) is estimated by considering the spin signal is in the linear regime with bias current, and from the spin signal presented in Fig. 1(e), $X = 1 - \frac{16}{272} = 0.94$, which alludes to 94% spin absorption by $TaTe_2$.

$\frac{\hat{I}s}{I_c}$ can be written as below.

$$\begin{aligned}
\frac{\hat{I}s}{I_c} &\equiv \frac{\int_0^{t_M} I_s(z)dz}{I_c t_{\rm TaTe_2}} \\
&= \frac{\lambda_{\rm TaTe_2}}{t_{\rm TaTe_2}}\frac{\left(1-e^{-\frac{t_{\rm TaTe_2}}{\lambda_{\rm TaTe_2}}}\right)^2}{1-e^{-2\frac{t_{\rm TaTe_2}}{\lambda_{\rm TaTe_2}}}}\frac{I_s(z=0)}{I_c} \\
&= \frac{\lambda_{\rm TaTe_2}}{t_{\rm TaTe_2}}\frac{\left(1-e^{-\frac{t_{\rm TaTe_2}}{\lambda_{\rm TaTe_2}}}\right)^2}{1-e^{-2\frac{t_{\rm TaTe_2}}{\lambda_{\rm TaTe_2}}}} \\
&\times \frac{2p_i Q_{IF1}\left[(2Q_{IF2}+1)(1-Q_{IM})e^{\frac{-L_{\rm SH}}{\lambda_{gr}}} - (1+Q_{IM})e^{\frac{-3L_{\rm SH}}{2\lambda_{gr}}}\right]}{(2Q_{IF1}+1)(2Q_{IF2}+1)(1+Q_{IM}) - (2Q_{IF1}+1)(1+Q_{IM})e^{\frac{-3L_{\rm SH}}{2\lambda_{gr}}} - (2Q_{IF2}+1)(1-Q_{IM})e^{\frac{-L_{\rm SH}}{\lambda_{gr}}} - (Q_{IM}-1)e^{\frac{-2L_{\rm SH}}{\lambda_{gr}}}}.
\end{aligned}$$

Here, $R_{gr} = \frac{R_{gr}\lambda_{gr}}{w_{gr}}$, $Q_{IFi} = \frac{1}{1-p^2}\frac{R_{ci}}{R_{gr}}$, with $I = 1, 2$, R_{ci} corresponding to injector and detector contact resistances, respectively. $Q_{IM} = \frac{w_{gr}R_{int.}}{R_{gr}\lambda_{gr}}$, $R_{\rm int}$, $w_g r$, R_{gr} are the $TaTe_2$-graphene interface resistance, graphene channel width, and square resistance, respectively, and are presented in Table I. As the spin diffusion length in $TaTe_2$ is an unknown parameter, we estimated spin Hall angle ($\theta_{\rm SH}$) as a function of spin

TABLE I. Parameters of graphene-$TaTe_2$ for device 3 to estimate the spin Hall angle in $TaTe_2$ to solve Eq. (E1).

	D_s (m^2/s)	τ_s (ps)	λ_{Gr} (μm)	w_{Gr} (μm)	$L_{\rm SH}$ (μm)	$t_{\rm TaTe_2}$ (nm)	$w_{\rm TaTe_2}$ (μm)	$R_{sq,Gr}$ (Ω)	$\rho_{\rm TaTe_2}$ (μΩ cm)	R_{c1} (kΩ)	R_{c2} (kΩ)
Device 1	0.021	311	2.56	1.8	2.5	70	2.6	339	300	20	15

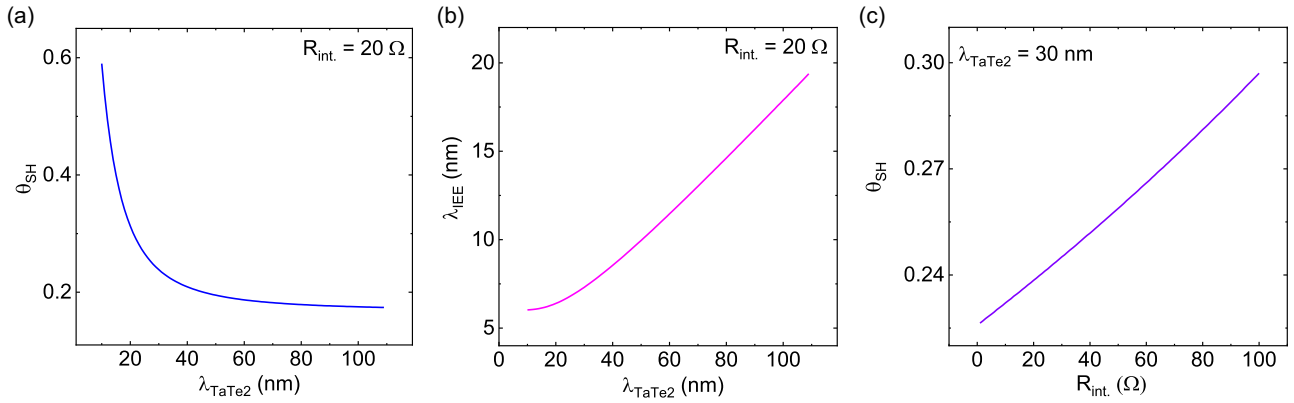

FIG. 9. Estimation of the spin Hall angle ($\theta_{\rm SH}$) in $TaTe_2$. (a) Spin Hall angle ($\theta_{\rm SH}$) as a function of spin diffusion length in $TaTe_2$ ($\lambda_{\rm TaTe_2}$) considering $R_{\rm int} = 20\,\Omega$. (b) IEE length ($\lambda_{\rm IEE}$) as a function of $\lambda_{\rm TaTe_2}$. (c) Spin Hall angle ($\theta_{\rm SH}$) as a function of $R_{\rm int}$ considering spin diffusion length $\lambda_{\rm TaTe_2} = 30\,$nm.

diffusion length ($\lambda_{\rm TaTe_2}$) in $TaTe_2$ by assuming $R_{\rm int} = 20\,\Omega$ [shown in Fig. 9(a)]. The spin Hall angle $\theta_{\rm SH}$ decays exponentially with increasing $\lambda_{\rm TaTe_2}$ according to Eq. (E1) and its simplified solution. We found $\theta_{\rm SH}$ is 0.59 at $\lambda_{\rm TaTe_2} = 10\,$nm; 0.23 at $\lambda_{\rm TaTe_2} = 30\,$nm, and becomes saturated with 0.20. We can also approximately calculate the inverse Edelstein effect (IEE) of $TaTe_2$ through IEE length $\lambda_{\rm IEE} = \theta_{\rm SH} * \lambda_{\rm TaTe_2}$, and we found $\lambda_{\rm IEE} \approx 6$–$60\,$nm [see Fig. 9(b)] as a function of $\lambda_{\rm TaTe_2}$ (10–110 nm) by considering $R_{\rm int} = 20\,\Omega$.

Overall, the calculated range of $\theta_{\rm SH}$ for $TaTe_2$ seems to be consistent with Pt ($\theta_{SH,Pt} \approx 0.23$) [10,11], and other TMDs such as $MoTe_2$ ($\theta_{SH,\rm MoTe2} \approx 0.2$) [38], MoS_2 ($\theta_{SH,\rm MoS2} \approx 0.1$) [17], but one order of magnitude higher compared to the lower limit of the $\theta_{SH,\rm WTe2}$ for WTe_2 ($\theta_{SH,\rm WTe2} = 0.01$) [12]. Interestingly, the estimated values of $\lambda_{\rm IEE}$ are comparable to topological insulators [52] (2.1 nm), oxide interfaces [53] (6.4 nm), but it seems to be one order of magnitude higher than in heavy metals (0.1–0.4 nm) and other Rashba systems [33,54]. Figure 9(c) depicts $\theta_{\rm SH}$ as a function of $R_{\rm int}$ by considering spin diffusion length in $TaTe_2$, $\lambda_{\rm TaTe_2} = 30\,$nm at room temperature. The spin Hall angle, $\theta_{\rm SH}$, shows a linear dependence on $R_{\rm int}$ and ranges from 0.22 to 0.29 for $R_{\rm int} = 1$–$100\,\Omega$.

APPENDIX F: SPIN TRANSPORT AND SPIN POLARIZATION IN GRAPHENE-$TaTe_2$ HETEROSTRUCTURE

We characterized the spin transport properties in the graphene-$TaTe_2$ channel (without spin absorption) to estimate the spin polarization of the detector FM contact. Figure 10 (a) shows the sketch of the measurement geometry for NL Hanle measurement, where the magnetic field is applied in the out-of-plane direction. The measured spin precession signal is fitted with the following Hanle precession Eq. (F1) to approximate the spin diffusion constant (D_s), spin diffusion length (λ_s), and lifetime (τ_s):

$$\Delta R_{\rm NL} \propto \int_0^\infty \frac{1}{\sqrt{4\pi Dt}} e^{-\frac{L^2}{4Dst}} \cos(\omega_L t)\, e^{\frac{-t}{\tau_s}} dt. \qquad \text{(F1)}$$

Furthermore, the measured Hanle spin signal (purple circles) along with its fit (magenta line) to Eq. (F2) is shown in Fig. 10(b) to extract TiO_2/Co contact polarization:

$$\Delta R_{\rm NL} = \pm \frac{P_i P_d R_{sq} D_s}{W} \,{\rm Re}\left\{ \frac{1}{2D_s} \frac{e^{-L\sqrt{\lambda_s^{-2} - i\frac{\omega}{D_s}}}}{\sqrt{\tau_s^{-1} - i\omega}} \right\}. \qquad \text{(F2)}$$

Here, ω depends on the frequency of spin flips and Larmor precession, $\omega_L = \frac{g\mu_B}{\hbar} B_\perp$ is the Larmor frequency, where $B_\perp$ is an applied perpendicular magnetic field to the easy axis of the FM contacts, $g = 2$ is assumed. In equation (F1) and (F2), D_s is the spin diffusion constant, and λ_s ($2.56 \pm 0.14\,\mu$m) and τ_s ($311 \pm 16\,$ps) are the spin diffusion length and spin lifetime, respectively. In device 1, $R_{sq} = 339\,\Omega$ for multilayer exfoliated graphene at $V_g = 40\,$V on Si/SiO_2 substrate. The distance between spin injection and spin detection electrodes is $L = 4.5\,\mu$m, graphene width, $w = 1.8\,\mu$m. Considering the spin polarization of the injector and detector to be equal ($P_i = P_d$), $P_{\rm Co/TiO2}$ is estimated to be about $6.13\% \pm 0.9\%$.

To estimate the current-induced spin polarization in $TaTe_2$ in device 2, we have also used the same equation, Eq. (F2), to fit the Hanle signal, as shown in Fig. 2(f). In device 2, using the graphene channel resistance, $R_{sq} = 1425\,\Omega$, width

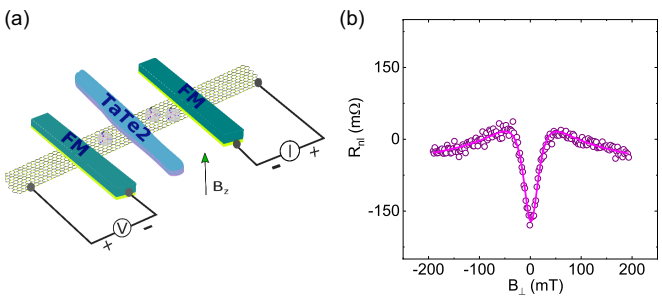

FIG. 10. Spin transport in the graphene-$TaTe_2$ heterostructure. (a) Sketch of the measurement setup for nonlocal Hanle measurement. (b) Hanle spin precession signal (violate circles) without spin absorption by $TaTe_2$ at back-gate voltage $V_g = 40\,$V with bias current $I = -30\,\mu$A along with the fitted line (magenta line) to Eq. (F2) to estimate the spin polarization of FM contacts.

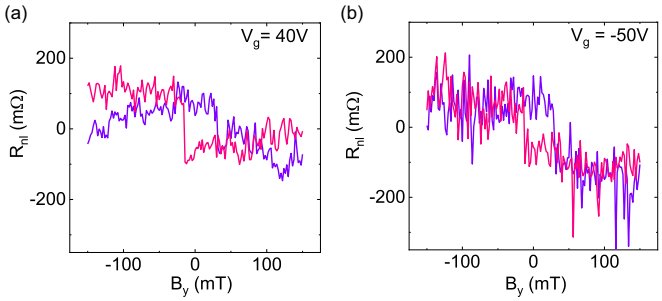

FIG. 11. Spin injection from $TaTe_2$ into graphene and spin-switch signal in device 1. (a, b) Spin injection from $TaTe_2$ into graphene for the electron- and hole-doped regimes at gate voltages $V_g = 40$ and -50 V with $I = -40$ and -30 μA, respectively.

$w = 1.2\,\mu$m, we found that

$$\sqrt{P_{\mathrm{TaTe_2}} P_{\mathrm{Co/TiO2}}} = 0.0287 \pm 0.0127$$

$$P_{\mathrm{TaTe_2}} = \frac{0.0287^2}{P_{\mathrm{Co/TiO2}}} \pm \frac{0.0127^2}{P_{\mathrm{Co/TiO2}}}$$

$$= 0.0134 \pm 0.0026\,.$$

Now, using previously obtained $P_{\mathrm{Co/TiO2}} = 6.13\%$, the spin polarization is of $TaTe_2$ is approximated to be $P_{\mathrm{TaTe_2}} = 1.34\% \pm 0.26\%$.

APPENDIX G: SPIN INJECTION FROM $TaTe_2$ INTO GRAPHENE IN DEVICE 1

The vertical spin injection results were reproducibly observed at room temperature in three different devices fabricated with similar methods, as presented in this manuscript. Figure 11 shows the spin injection from $TaTe_2$ into graphene and spinswitch signal in device 1. The possibility of spin transport contribution from the reference FM electrodes on the graphene channel in the injector and detector circuit can be ruled out, as it would have resulted in multiple switches in the measured signal (see Fig. 1(e), where both FM injector and detector contacts are involved in the conventional spin-valve measurements).

APPENDIX H: CURRENT-INDUCED SPIN POLARIZATION IN SYMMETRIC AND LOW-SYMMETRIC CRYSTALS

Here we discuss possible origins of in-plane spin polarization in $TaTe_2$ considering the crystal structure of $TaTe_2$. 1T'-$TaTe_2$ is a centrosymmetric layered material at room temperature where spin current (I_s), charge current (I_c), and spin polarization (s) are perpendicular to each other for symmetric measurements of the spin Hall effect (SHE) or Edelstein effect (EE). To facilitate our discussion, three-dimensional (3D) axis directions are presented in Fig. 12(a), similar to the schematics shown in Figs. 2(a) and 2(d). Conventional ISHE in the symmetric 3D crystal of $TaTe_2$ is shown in Fig. 12(b), where I_s, I_c, and s are perpendicular to each other in the z, y, and x directions, respectively, and can explain the measurements depicted in Figs. 2(a)–2(c).

Interestingly, in-plane spin polarization along the y axis in $TaTe_2$, presented in Figs. 2(d)–2(f), is possible while injecting charge current (I_c) can be along the z axis [Fig. 12(c)] and x axis [Fig. 12(d)], which needs to be perpendicular to the corresponding spin current (I_s) to maintain symmetry. These symmetries allow bulk and surface states to inject spin from bulk (via SHE) or surface states (via Edelstein effect) of $TaTe_2$. While charge current (I_c) and spin current (I_s) are along the z axis and x axis, respectively, the spins are accumulated at the edges of $TaTe_2$ [Fig. 12(c)]. However, the $TaTe_2$ crystals have a relatively smaller thickness (70–100 nm) and

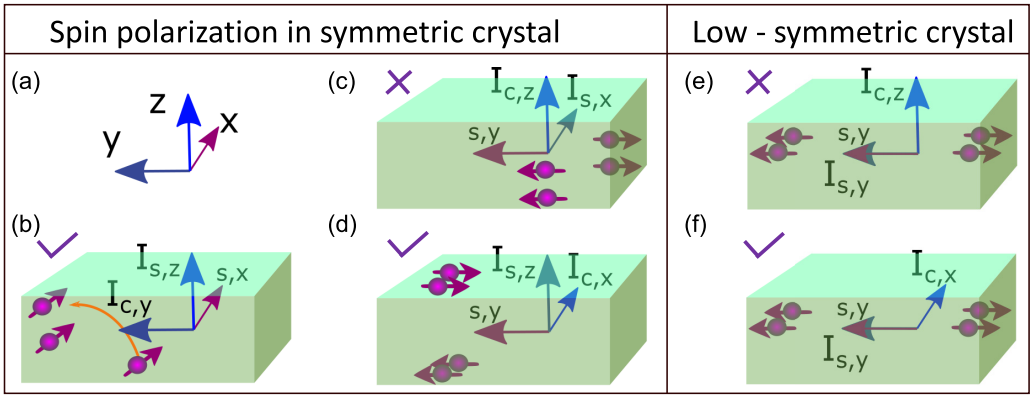

FIG. 12. (a) The x, y, and z-axis directions similar to the schematics shown in Figs. 2(a) and 2(d) to explain three-dimensional crystal symmetry. (b) Spin to charge conversion due to inverse spin Hall effect (ISHE), shown in Figs. 2(a)–2(c) in the high-symmetry crystal structure, where spin absorption in $TaTe_2$ renders z-direction spin current ($I_{s,z}$) with the spin direction along the x axis (s_x) and measured charge current in the y axis ($I_{c,y}$). (c) Spin polarization in symmetric $TaTe_2$ to explain the spin-switch measurements shown in Figs. 2(d)–2(f). In this case, injected spin current in graphene is along the y direction, and keeping this in mind, we have two possible scenarios. First, charge current and spin current are out of plane (along the z axis) and in plane (along the x axis), respectively, and spins are accumulated at the edges of $TaTe_2$. In the second scenario, shown in (d), where spin along the y direction is accumulated at the top and bottom surface of $TaTe_2$ and charge current and spin current are in x and z direction. (e, f) Spin polarization and spin current are parallel and along the y axis in lower symmetry situations but perpendicular to the charge current, which can be in the z or x axis, respectively.

negligible edge area in contact with graphene compared to the bottom surface area. Hence, in-plane (y-axis) spin injection into graphene from the accumulated spins at the $TaTe_2$ edges is improbable. On the other hand, considering charge current (I_c) and spin current (I_s) are along the x and z axis [Fig. 12(d)], where spin along the y axis can accumulate at the top and bottom surface of $TaTe_2$, this can explain our measurements of spin polarization in symmetric $TaTe_2$ crystal with lateral widths of 2.6–6 μm in contact with graphene and nanometer-range thickness.

However, in-plane spin polarization can also emerge in unconventional and lower symmetric $TaTe_2$ crystal [see Figs. 12(e) and 12(f)], where spin current and spin orientation can be parallel to each other and along the y axis ($s \parallel I_s$) but are perpendicular to the charge current (I_c), which could be in either z or x direction in our measurement geometry [45]. Again, considering k-dependent spin polarization and the lateral width of $TaTe_2$, which is considerably higher than the thickness, the latter situation is more likely to emanate in such a lower symmetric crystal because of SHE or EE.

[1] W. Han, R. K. Kawakami, M. Gmitra, and J. Fabian, Graphene spintronics, Nat. Nanotechnol. **9**, 794 (2014).

[2] I. Žutić, J. Fabian, and S. Das Sarma, Spintronics: Fundamentals and applications, Rev. Mod. Phys. **76**, 323 (2004).

[3] D. D. Awschalom and M. E. Flatté, Challenges for semiconductor spintronics, Nat. Phys. **3**, 153 (2007).

[4] A. Fert, Origin, development, and future of spintronics (Nobel lecture), Angew Chemie Int. Ed. **47**, 5956 (2008).

[5] A. Manchon, J. Železný, I. M. Miron, T. Jungwirth, J. Sinova, A. Thiaville, K. Garello, and P. Gambardella, Current-induced spin-orbit torques in ferromagnetic and antiferromagnetic systems, Rev. Mod. Phys. **91**, 035004 (2019).

[6] K. Garello, F. Yasin, H. Hody, S. Couet, L. Souriau, S. H. Sharifi, J. Swerts, R. Carpenter, S. Rao, W. Kim *et al.*, Manufacturable 300 mm platform solution for Field-Free Switching SOT-MRAM, 2019 *Symposium on VLSI Technology* (Kyoto, Japan, 2019), pp. T194-T195.

[7] J. Sinova, S. O. Valenzuela, J. Wunderlich, C. H. Back, and T. Jungwirth, Spin Hall effects, Rev. Mod. Phys. **87**, 1213 (2015).

[8] A. Manchon, H. C. Koo, J. Nitta, S. M. Frolov, and R. A. Duine, New perspectives for Rashba spin-orbit coupling, Nat. Mater. **14**, 871 (2015).

[9] J. C. Rojas-Sánchez and A. Fert, Compared Efficiencies of Conversions between Charge and Spin Current by Spin-Orbit Interactions in Two- and Three-Dimensional Systems, Phys. Rev. Appl. **11**, 054049 (2019).

[10] W. S. Torres, J. F. Sierra, L. A. Benítez, F. Bonell, M. V. Costache, and S. O. Valenzuela, Spin precession and spin Hall effect in monolayer graphene/Pt nanostructures, 2D Mater. **4**, 041008 (2017).

[11] W. Yan, E. Sagasta, M. Ribeiro, Y. Niimi, L. E. Hueso, and F. Casanova, Large room temperature spin-to-charge conversion signals in a few-layer graphene/Pt lateral heterostructure, Nat. Commun. **8**, 661 (2017).

[12] B. Zhao, D. Khokhriakov, Y. Zhang, H. Fu, B. Karpiak, A. Md. Hoque, X. Xu, Y. Jiang, B. Yan, and S. P. Dash, Observation of charge to spin conversion in Weyl semimetal WTe2 at room temperature, Phys. Rev. Res. **2**, 013286 (2020).

[13] B. Zhao, B. Karpiak, D. Khokhriakov, A. M. Hoque, X. Xu, Y. Jiang, and S. P. Dash, Edelstein effect in type-II Weyl semimetal WTe2 up to room temperature, arXiv:1910.06225.

[14] Z. Kovács-Krausz, A. M. Hoque, P. Makk, B. Szentpéteri, M. Kocsis, B. Fülöp, M. V. Yakushev, T. V. Kuznetsova, O. E. Tereshchenko, K. A. Kokh *et al.*, Electrically controlled spin injection from giant Rashba spin-orbit conductor BiTeBr, Nano Lett. **20**, 4782 (2020).

[15] L. Li, J. Zhang, G. Myeong, W. Shin, H. Lim, B. Kim, S. Kim, T. Jin, S. Cavill, B. S. Kim *et al.*, Gate-tunable reversible Rashba-Edelstein effect in a few-layer graphene/2H-TaS_2 heterostructure at room temperature, ACS Nano **14**, 5251 (2020).

[16] T. S. Ghiasi, A. A. Kaverzin, P. J. Blah, and B. J. van Wees, Charge-to-spin conversion by the Rashba-Edelstein effect in two-dimensional van der Waals heterostructures up to room temperature, Nano Lett. **19**, 5959 (2019).

[17] C. K. Safeer, J. Ingla-Aynés, F. Herling, J. H. Garcia, M. Vila, N. Ontoso, M. R. Calvo, S. Roche, L. E. Hueso, and F. Casanova, Room-temperature spin Hall effect in graphene/MoS_2 van der Waals heterostructures, Nano Lett. **19**, 1074 (2019).

[18] D. Khokhriakov, A. W. Cummings, K. Song, M. Vila, B. Karpiak, A. Dankert, S. Roche, and S. P. Dash, Tailoring emergent spin phenomena in Dirac material heterostructures, Sci. Adv. **4**, eaat9349 (2018).

[19] C. H. Li, O. M. J. van't Erve, J. T. Robinson, Y. Liu, L. Li, and B. T. Jonker, Electrical detection of charge-current-induced spin polarization due to spin-momentum locking in Bi_2Se_3, Nat. Nanotechnol. **9**, 218 (2014).

[20] A. Dankert, J. Geurs, M. V. Kamalakar, S. Charpentier, and S. P. Dash, Room temperature electrical detection of spin polarized currents in topological insulators, Nano Lett. **15**, 7976 (2015).

[21] A. Dankert, P. Bhaskar, D. Khokhriakov, I. H. Rodrigues, B. Karpiak, M. V. Kamalakar, S. Charpentier, I. Garate, and S. P. Dash, Origin and evolution of surface spin current in topological insulators, Phys. Rev. B **97**, 125414 (2018).

[22] N. H. D. Khang, Y. Ueda, and P. N. Hai, A conductive topological insulator with large spin Hall effect for ultralow power spin-orbit torque switching, Nat. Mater. **17**, 808 (2018).

[23] A. R. Mellnik, J. S. Lee, A. Richardella, J. L. Grab, P. J. Mintun, M. H. Fischer, A. Vaezi, A. Manchon, E. A. Kim, N. Samarth, and D. C. Ralph, Spin-transfer torque generated by a topological insulator, Nature (London) **511**, 449 (2014).

[24] D. C. Manendra, R. Grassi, J.-Y. Chen, M. Jamali, D. R. Hickey, D. Zhang, Z. Zhao, H. Li, P. Quarterman, Y. Lv, M. Li, A. Manchon, K. A. Mkhoyan, T. Low, and J.-P. Wang, Room-temperature high spin-orbit torque due to quantum confinement in sputtered $Bi_xSe_{(1-x)}$ films, Nat. Mater. **17**, 800 (2018).

[25] J. A. Voerman, C. Li, Y. Huang, and A. Brinkman, Spin-momentum locking in the gate tunable topological insulator $BiSbTeSe_2$ in non-local transport measurements, Adv. Electron. Mater. **5**, 1900334 (2019).

[26] K. Vaklinova, A. Hoyer, M. Burghard, and K. Kern, Current-induced spin polarization in topological insulator-graphene heterostructures, Nano Lett. **16**, 2595 (2016).

[27] B. Zhao, D. Khokhriakov, B. Karpiak, A. M. Hoque, L. Xu, L. Shen, Y. P. Feng, X. Xu, Y. Jiang, and S. P. Dash, Electrically controlled spin-switch and evolution of Hanle spin precession in graphene, 2D Mater. **6**, 035042 (2019).

[28] A. H. Castro Neto and F. Guinea, Impurity-Induced Spin-Orbit Coupling in Graphene, Phys. Rev. Lett. **103**, 026804 (2009).

[29] B. Karpiak, A. W. Cummings, K. Zollner, M. Vila, D. Khokhriakov, A. M. Hoque, A. Dankert, P. Svedlindh, J. Fabian, S. Roche, and S. P. Dash, Magnetic proximity in a van der Waals heterostructure of magnetic insulator and graphene, 2D Mater. **7**, 015026 (2020).

[30] S. Manipatruni, D. E. Nikonov, C.-C. Lin, T. A. Gosavi, H. Liu, B. Prasad, Y.-L. Huang, E. Bonturim, R. Ramesh, and I. A. Young, Scalable energy-efficient magnetoelectric spin-orbit logic, Nature (London) **565**, 35 (2019).

[31] J. J. Gao, J. G. Si, X. Luo, J. Yan, F. C. Chen, G. T. Lin, L. Hu, R. R. Zhang, P. Tong, W. H. Song, X. B. Zhu, W. J. Lu, and Y. P. Sun, Origin of the structural phase transition in single-crystal $TaTe_2$, Phys. Rev. B **98**, 224104 (2018).

[32] M. Milletarì, M. Offidani, A. Ferreira, and R. Raimondi, Covariant Conservation Laws and the Spin Hall Effect in Dirac-Rashba Systems, Phys. Rev. Lett. **119**, 246801 (2017).

[33] J. C. R. Sánchez, L. Vila, G. Desfonds, S. Gambarelli, J. P. Attané, J. M. De Teresa, C. Magén, and A. Fert, Spin-to-charge conversion using Rashba coupling at the interface between non-magnetic materials, Nat. Commun. **4**, 2944 (2013).

[34] M. Offidani, M. Milletarì, R. Raimondi, and A. Ferreira, Optimal Charge-to-Spin Conversion in Graphene on Transition-Metal Dichalcogenides, Phys. Rev. Lett. **119**, 196801 (2017).

[35] M. V. Kamalakar, A. Dankert, P. J. Kelly, and S. P. Dash, Inversion of spin signal and spin filtering in ferromagnet|hexagonal boron nitride-graphene van der Waals heterostructures, Sci. Rep. **6**, 21168 (2016).

[36] D. Khokhriakov, B. Karpiak, A. M. Hoque, and S. P. Dash, Two-dimensional spintronic circuit architectures on large scale graphene, Carbon **161**, 892 (2020).

[37] J. Zhang, B. Yang, H. Zheng, X. Han, and Y. Yan, Large magnetic anisotropy and strain induced enhancement of magnetic anisotropy in monolayer $TaTe_2$, Phys. Chem. Chem. Phys. **19**, 24341 (2017).

[38] C. K. Safeer, N. Ontoso, J. Ingla-Aynés, F. Herling, V. T. Pham, A. Kurzmann, K. Ensslin, A. Chuvilin, I. Robredo, M. G. Vergniory *et al.*, Large multidirectional spin-to-charge conversion in low-symmetry semimetal $MoTe_2$ at room temperature, Nano Lett. **19**, 8758 (2019).

[39] S. O. Valenzuela and M. Tinkham, Direct electronic measurement of the spin Hall effect, Nature (London) **442**, 176 (2006).

[40] G. M. Stiehl, D. MacNeill, N. Sivadas, I. El Baggari, M. H. Guimarães, N. D. Reynolds, L. F. Kourkoutis, C. J. Fennie, R. A. Buhrman, and D. C. Ralph, Current-induced torques with Dresselhaus symmetry due to resistance anisotropy in 2D materials, ACS nano **13**, 2599 (2019).

[41] B. Karpiak, A. Dankert, A. W. Cummings, S. R. Power, S. Roche, and S. P. Dash, 1D ferromagnetic edge contacts to 2D graphene/h-BN heterostructures, 2D Mater. **5**, 014001 (2018).

[42] R. S. Patel, S. P. Dash, M. P. De Jong, and R. Jansen, Magnetic tunnel contacts to silicon with low-work-function ytterbium nanolayers, J. Appl. Phys. **106**, 016107 (2009).

[43] S. Sharma, S. P. Dash, H. Saito, S. Yuasa, B. J. van Wees, and R. Jansen, Anisotropy of spin polarization and spin accumulation in Si/Al_2O_3/ferromagnet tunnel devices, Phys. Rev. B **86**, 165308 (2012).

[44] A. Fert and H. Jaffrès, Conditions for efficient spin injection from a ferromagnetic metal into a semiconductor, Phys. Rev. B **64**, 184420 (2001).

[45] D. Culcer and R. Winkler, Generation of Spin Currents and Spin Densities in Systems with Reduced Symmetry, Phys. Rev. Lett. **99**, 226601 (2007).

[46] A. Dankert and S. P. Dash, Electrical gate control of spin current in van der Waals heterostructures at room temperature, Nat. Commun. **8**, 16093 (2017).

[47] D. Khokhriakov, A. M. Hoque, B. Karpiak, and S. P. Dash, Gate-tunable spin-galvanic effect in graphene-topological insulator van der Waals heterostructures at room temperature, Nature Commun. **11**, 1 (2020).

[48] A. M. Hoque, D. Khokhriakov, B. Karpiak, and S. P. Dash, All-electrical creation and control of giant spin-galvanic effect in 1T-$MoTe_2$/graphene heterostructures at room temperature, arXiv:1908.09367v2.

[49] L. A. Benítez, W. S. Torres, J. F. Sierra, M. Timmermans, J. H. Garcia, S. Roche, M. V. Costache, and S. O. Valenzuela, Tunable room-temperature spin galvanic and spin Hall effects in van der Waals heterostructures, Nat. Mater. **19**, 170 (2020).

[50] X. Zhang, Q. Liu, J.-W. Luo, A. J. Freeman, and A. Zunger, Hidden spin polarization in inversion-symmetric bulk crystals, Nat. Phys. **10**, 387 (2014).

[51] J.-C. Rojas Sánchez, P. Laczkowski, W. F. Savero Torres, M. Cubukcu, V. D. Nguyen, L. Notin, C. Beigné, C. Vergnaud, A. Marty, M. Jamet, L. Vila, and J. P. Attané, In-plane and out-of-plane spin precession in lateral spin-valves, Appl. Phys. Lett. **102**, 132408 (2013).

[52] J.-C. Rojas-Sánchez, S. Oyarzún, Y. Fu, A. Marty, C. Vergnaud, S. Gambarelli, L. Vila, M. Jamet, Y. Ohtsubo, A. Taleb-Ibrahimi *et al.*, Spin to Charge Conversion at Room Temperature by Spin Pumping into a New Type of Topological Insulator: α-Sn Films, Phys. Rev. Lett. **116**, 096602 (2016).

[53] E. Lesne, Y. Fu, S. Oyarzun, J. C. Rojas-Sánchez, D. C. Vaz, H. Naganuma, G. Sicoli, J.-P. Attané, M. Jamet, E. Jacquet *et al.*, Highly efficient and tunable spin-to-charge conversion through Rashba coupling at oxide interfaces, Nat. Mater. **15**, 1261 (2016).

[54] A. Nomura, T. Tashiro, H. Nakayama, and K. Ando, Temperature dependence of inverse Rashba-Edelstein effect at metallic interface, Appl. Phys. Lett. **106**, 212403 (2015).